NPG Asia Materials (2017) 9, e416; doi:10.1038/am.2017.141
www.nature.com/am

ORIGINAL ARTICLE

Easy on-demand self-assembly of lateral nanodimensional hybrid graphene oxide flakes for near-infrared-induced chemothermal therapy

Raj Kumar Thapa[1], Jeong Hoon Byeon[2], Sae Kwang Ku[3], Chul Soon Yong[1] and Jong Oh Kim[1]

Near-infrared (NIR)-induced chemothermal doxorubicin (DOX) release for anticancer activity was demonstrated using DOX-incorporated fully lateral nanodimensional graphene oxide (nGO) flakes layered with chitosan-polyethylene glycol (PEG) conjugate (nGO@DOX-cPEG) from a single-pass gas-phase self-assembly. Unlike most previously reported graphene oxide-based drug carriers, the proposed processing method introduced a fully nanoscale (both in lateral dimension and thickness) configuration without multistep wet physicochemical processes that enhance the drug-loading capacity and NIR-induced heat generation resulting from the increased surface area. The accumulation of nGO@DOX-cPEG flakes in prostate cancer cells enhanced apoptotic phenomena via the combined effects of DOX release and heat generation upon NIR irradiation. The combined anticancer effects were verified through *in vivo* assessment with better safety profiles than free DOX. The proposed strategy warrants continuous assembly of multimodal nanocarriers for the efficient treatment of prostate cancers and may be a promising candidate for advanced drug delivery systems.

NPG Asia Materials (2017) **9,** e416; doi:10.1038/am.2017.141; published online 4 August 2017

INTRODUCTION

Chemotherapy for cancer treatment has several serious limitations, such as toxicity, cancer recurrence and drug resistance; thus, realizable alternative therapeutic approaches must be developed to secure their efficacy and safety.[1,2] In the past 20 years, tremendous efforts have been undertaken to utilize nanotechnology-based drug delivery systems to resolve these issues and improve the therapeutic efficacy for optimal cancer treatments.[3–5] Drug release in combination with hyperthermia therapy can efficiently kill cancer cells in a specific tumor region, thereby minimizing damage to normal healthy tissues.[6] Near-infrared (NIR) laser irradiation can penetrate into deeper tissue layers without any damage to cells because of its wavelength range (650–900 nm).[7] This property can be utilized on tumor-targeted carbon- or gold-based nanomaterials, which can efficiently absorb NIR for cell death induction via hyperthermia therapies in the localized irradiation area.[6]

Graphene oxide (GO) has recently been used as a promising carbonaceous material for photo-assisted therapeutic applications. GO has been used for biosensor and diagnostic applications because of its excellent physical and chemical properties (for example, high electrical conductivity, strength and large surface area for drug loading).[8,9] Two-dimensional GO flakes possess great potential for enhanced drug delivery through conjugation with proteins, fluorescent probes, drugs and protective coatings to their surface-available functional groups.[10–14] As a complementary means, polyethylene glycol (PEG) incorporation with graphenes has been found to effectively kill cancer cells with minimum adverse effects for practical applications in drug delivery systems.[15–18]

The lateral dimension, thickness and shape of GO flakes can potentially affect the therapeutic outcomes.[19,20] Cellular uptake of exogenous species smaller than 1 μm generally occurs through endocytosis (caveolae- or clathrin-mediated); otherwise, cellular uptake occurs via phagocytosis or micropinocytosis.[21] A previous report explored size-dependent internalization of GO[22] and the results suggested that controlling lateral dimensions may optimize therapeutic efficacies. However, the incorporation of drugs and/or biofunctional coatings on GO surfaces generally requires multiple preparation steps and tedious chemical reactions and separations. Therefore, simple, continuous and efficient methodologies for the on-demand fabrication of GO-based biofunctional platforms are necessary. Securing a fully lateral nanodimensional (both the lateral dimension and thickness) configuration may enhance cellular internalization to introduce beneficial biomedical applications. In this study, we designed and prepared a novel system to self-assemble fully lateral nanodimensional GO (nGO)-incorporated doxorubicin (DOX) (nGO@DOX) flakes in a single-pass reaction condition. An nGO flake-laden nitrogen gas flow

---

[1]College of Pharmacy, Yeungnam University, Gyeongsangbuk-do, Gyeongsan, Republic of Korea; [2]School of Mechanical Engineering, Yeungnam University, Gyeongsan, Republic of Korea and [3]College of Korean Medicine, Daegu Haany University, Gyeongsan, Republic of Korea
Correspondence: Professor JH Byeon or CS Yong or JO Kim, School of Mechanical Engineering, Yeungnam University, 280 Daehak-ro, Gyeongsangbuk-do, Gyeongsan 38541, Republic of Korea.
E-mail: postjb@yu.ac.kr
or CS Yong or JO Kim, College of Pharmacy, Yeungnam University, Gyeongsangbuk-do, Gyeongsan 38541, Republic of Korea.
E-mail: csyong@yu.ac.kr or jongohkim@yu.ac.kr

Received 4 October 2016; revised 1 June 2017; accepted 4 June 2017

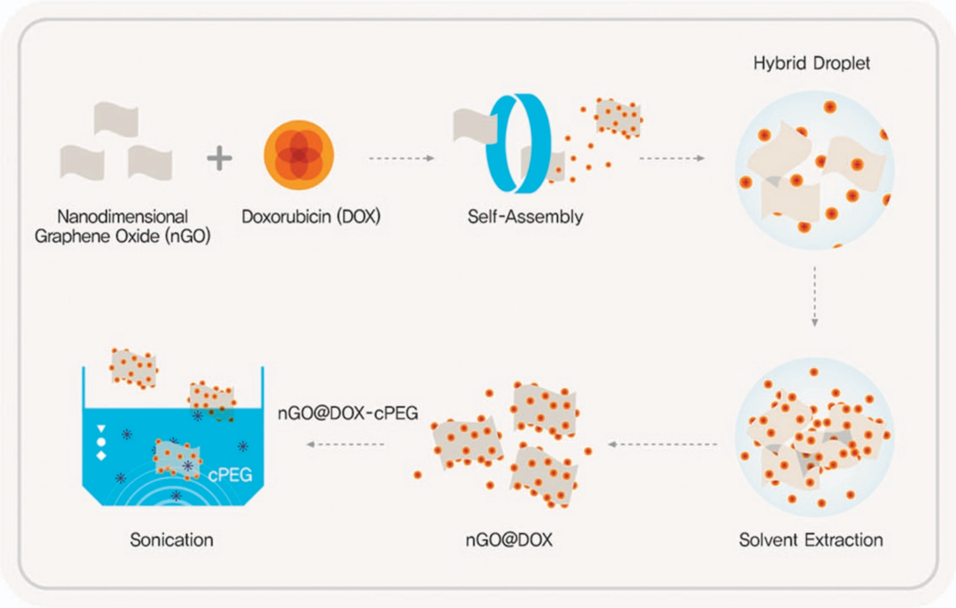

Figure 1 Single-pass gas-phase self-assembly of nanodimensional graphene oxide (nGO)-incorporated doxorubicin (DOX) (nGO@DOX) flakes from incorporation of nGO flakes and DOX droplets and subsequent solvent extraction from the hybrid droplets. The assembled nGO@DOX flakes were incorporated with chitosan-polyethylene glycol (cPEG) in the liquid phase before application in anticancer activity analysis.

from graphite nanoparticle precursors was directly injected into DOX droplets (DOX dissolved in ethanol) in a collison atomizer and heat-treated (<90 °C wall temperature) to liberate the solvent from the droplets, resulting in the formation of nGO@DOX flakes (refer to Supplementary Figure S1). The assembled flakes were mechanically collected on hydrophobic substrates to evaluate their potential anticancer activity. The prepared flakes on the substrate were incorporated with a chitosan-PEG (cPEG) solution to form nGO@DOX-cPEG flakes (Figure 1) before *in vitro* and *in vivo* assessments for proving NIR-induced chemothermal activity to prostate cancers.

MATERIALS AND METHODS

Preparation

Graphite nanoparticles were produced via spark discharge[23] and carried by nitrogen gas (99.9999% purity, $3\,\mathrm{l\,min^{-1}}$) to an impinging device, as shown in Supplementary Figure S1. The specifications of the discharge configuration were as follows: electrode diameter (C-072561, Nilaco, Japan) and length, 3 and 100 mm, respectively; resistance, 0.5 MΩ; capacitance, 1.0 nF; loading current, 2.0 mA; applied voltage, 3.0 kV; and frequency, 667 Hz. The impinging device, which contained a simplified Hummer's solution[24] and an ultrasound probe, was used to collect the graphite particles into the solution and react with the solution to form nGO. The graphite particles experienced ultrasound ($250\,\mathrm{W\,cm^{-2}}$ intensity) when they reached the gas (the graphite particle-laden flow)–liquid (the simplified Hummer's solution in the impinging device) interface. nGO was obtained by oxidation of the graphite particles (which acted as precursors) with 40 ml of H_2SO_4 and 1.8 g of $KMnO_4$. The residence time of the graphite particles in the impinging device was 3.8 min to form nGO. The solution containing nGO was injected into the reservoir of a collison atomizer using a peristaltic pump (323Du/MC4, Watson-Marlow Bredel Pump, Wilmington, MA, USA). Another nitrogen gas flow was used as the operating gas for atomizing (collison atomizer 1) the nGO solution supplied by the pump to form nGO droplets. The droplets were then passed through a denuder containing activated carbon pellets and silica gels to drive solvent from the droplets. After passing through the denuder, the nGO-laden flow was directly used to atomize (collison atomizer 2) the DOX (1225703, Sigma-Aldrich, St Louis, MO, USA) solution ($1\,\mathrm{mg\,DOX\,ml^{-1}}$ ethanol). The nGO@DOX hybrid droplets were passed through a heated tubular reactor with a 90 °C wall temperature to extract the solvents from the droplets, resulting in nGO@DOX flakes. The flakes were mechanically collected on polytetrafluorotethylene substrates to evaluate their ability in chemothermal anticancer activity. To prevent unwanted agglomeration and hydrolysis of nGO@DOX flakes (if they are stored in aqueous solution as dispersion), the assembled flakes on a polytetrafluorotethylene substrate (that is, dried form) were incorporated with cPEG solution[25] just before the *in vitro* and *in vivo* assessments of stability and biosafety. Briefly, nGO@DOX flakes were first added to distilled water to form aqueous dispersions at chosen concentrations. Different amounts of cPEG were added to the nGO@DOX dispersion before vortexing and sonicating for 5 min to form nGO@DOX-cPEG flakes.

Characterization

Physicochemical properties of nGO@DOX and nGO@DOX-cPEG flakes. The light absorption properties of nGO and nGO@DOX flakes including DOX were analyzed using an ultraviolet–visible (UV–Vis) spectrophotometer (U-2800, PerkinElmer, Waltham, MA, USA). A morphological analysis of the prepared nGO and nGO@DOX-cPEG flakes was performed using transmission electron microscopy (H7600, Hitachi, Tokyo, Japan). Briefly, each of the prepared dispersions was added to a carbon-coated copper grid and dried under particle-free atmosphere before transmission electron microscopy analysis. Similarly, nGO and nGO@DOX-cPEG flake-deposited ultraflat mica square plates (Ted Pella, Inc., Redding, CA, USA) were used for atomic force microscopy analysis with a Nanoscope IIIa Scanning Probe Microscope (New Jersey Institute of Technology, Newark, NJ, USA). In addition, Fourier transform infrared analyses of dried nGO, DOX and nGO@DOX were performed using a Thermo Scientific Nicolet Nexus 670 Fourier transform infrared spectrophotometer (Thermo Fischer Scientific, Waltham, MA, USA). To examine the textural properties, the nGO flakes in gas phase were directly deposited on ultraflat silicon substrates using an electrostatic aerosol sampler (NPC-10, HCT, Icheon, South Korea) at an applied voltage of 5 kV. The N_2 adsorption isotherms of nGO and microdimensional GO (commercially available) flakes (0.2 g each) were measured using a porosimeter (ASAP 2010, Micromeritics Inc. Corp., Norcross, GA, USA) at 77.4 K at relative pressures ranging from 10^{-6} to 1. High-purity (99.9999%) N_2 was used. The GO flakes were out-gassed at 573 K for 2 h before each measurement. The specific surface area was determined using the Brunauer–Emmett–Teller equation.[26] The total pore volume was estimated based on the N_2 volume adsorbed at a relative saturation pressure (~0.996).

Determination of entrapment efficiency and loading capacity of DOX. The DOX entrapment in nGO@DOX and nGO@DOX-cPEG flakes was calculated by determining the free and total drug concentrations in the aqueous dispersion. Briefly, nGO@DOX or nGO@DOX-cPEG dispersions were filtered using an Amicon centrifugal ultrafiltration device (molecular weight cut-off (MWCO) 10 000 Da, Millipore, Billerica, MA, USA) for 10 min at 5000 r.p.m. The DOX concentration was determined using a high-performance liquid chromatography system (Hitachi) comprising an L-2130 pump, L-2200 autosampler, L-2420 UV–Vis detector and L-2350 column oven with Ezchrom elite software (318a, Hitachi, Tokyo, Japan). An Inertsil C_{18} column (150 mm × 4.6 mm, 5 μm particle size, Cosmosil, Nacalai Tesque Inc., San Diego, CA, USA) was used to perform isocratic elution with a mobile phase consisting of methanol: acetonitrile:acetic acid (1%) at 50:49:1 (v/v/v), a flow rate of 1.0 ml min^{-1} and column temperature of 25 °C. A 20 μl sample was injected for each analysis, and UV absorbance was measured at a wavelength of 254 nm. The entrapment efficiency (EE; %) was determined using the following formula:

$$\mathrm{EE}(\%) = \frac{W_{\mathrm{GO}}}{W_{\mathrm{T}}} \times 100$$

where W_{GO} is the weight of the DOX entrapped in the nGO and W_{T} is the total DOX added to the nGO dispersion.

The loading capacity (LC; %) was determined using the following formula:

$$\mathrm{LC}(\%) = \frac{W_{\mathrm{TD}} - W_{\mathrm{UD}}}{W_{\mathrm{TG}}} \times 100$$

where W_{TD}, W_{UD} and W_{TG} are the weights of total DOX, unbound DOX and total nGO, respectively.

In vitro drug release. In vitro release of DOX from nGO@DOX-cPEG flakes was determined using the dialysis method. Desired volumes of nGO@DOX-cPEG flakes were placed into dialysis membrane tubing (Spectra/Por, MWCO 3500 Da, Spectrum Laboratories, Inc., Rancho Dominguez, CA, USA) and immersed into 30 ml of phosphate-buffered saline (PBS, pH 7.4, 0.14 M NaCl) or acetate-buffered saline (pH 5.5, 0.14 M NaCl). At predetermined time intervals, 1 ml of samples were withdrawn and replaced with fresh media maintained at 37 °C. The amount of released DOX was determined using the previously described high-performance liquid chromatography method.

Biological assessment

Cell viability assay. In vitro cell viabilities for PC3, DU145 and LNCaP cells following treatments with nGO@cPEG and nGO@DOX-cPEG flakes including free DOX, with or without NIR irradiation, were determined using the 3-(4,5-dimethylthiazol-2-yl)-5-(3-carboxymethoxyphenyl)-2-(4-sulfophenyl)-2H-tetrazolium (MTS) assay (Promega, Madison, WI, USA). Prostate cancer cells were separately seeded in 96-well plates (1×10^4 cells per well) and incubated for 48 h. The cells were then treated with nGO@cPEG and nGO@DOX-cPEG flakes including free DOX, with or without NIR irradiation and incubated for 24 h. For all the treatments, an identical DOX concentration (1 μM) was used. The mass concentration of nGO@cPEG was same as that of the nGO@DOX-cPEG for relevant comparison. After incubation for 24 h, MTS solution was added to each treatment well, and the absorbance at 493 nm was measured using an automated microplate reader (Multiskan EX, Thermo Scientific, Waltham, MA, USA) to determine the cell viability.

Cellular uptake study. PC3, DU145 and LNCaP cells (2×10^4 cells per well) were seeded on coverslips placed in 12-well plates and incubated for 48 h. nGO@DOX-cPEG flakes were added to each well and incubated for 30 min. The cells were then washed with PBS solution and fixed with a 4% paraformaldehyde solution in the dark. The cells were washed with PBS solution, and the coverslip was mounted on a glass slide, sealed with glycerin and observed using a confocal laser scanning microscope (Leica TCS SP8 STED 3X, Leica Microsystems Ltd., Wetzlar, Germany). To quantitatively measure the cellular uptake, PC3, DU145 and LNCaP cells (1×10^5 cells per well) were seeded in 12-well plates and incubated for 48 h. The cells were treated with nGO@DOX-cPEG flakes at 5 μg ml^{-1} in a humidified incubator with 5% CO_2 at 37 °C. After 60 min incubation, the cells were washed with PBS solution and collected. The cells were then dispersed in 1.0 ml of PBS solution for flow cytometric measurements using a FACSCalibur flow cytometer (BD Biosciences, San Jose, CA, USA).

Apoptosis assay. PC3, DU145 and LNCaP cells were seeded in 12-well plates (1×10^5 cells per well), incubated for 48 h and treated with nGO@cPEG and nGO@DOX-cPEG flakes including free DOX, with or without NIR irradiation, for an additional 24 h. The cells were collected, washed with PBS solution, mixed with 1X Annexin-V-binding buffer and stained with Annexin-V and 7AAD for 10 min in the dark. The cells were diluted with binding buffer and analyzed for apoptosis using a FACSCalibur flow cytometer (BD Biosciences).

NIR-induced chemothermal activity. The effect of NIR irradiation on temperature elevations was analyzed by exposing nGO and nGO@DOX-cPEG flakes to NIR (2.0 W cm^{-2}) for 5 min. The temperature changes were digitally photographed using a thermal camera (Therm-App TH, Karmiel, Israel). The effect of NIR irradiation on the cell viability of nGO@cPEG and nGO@DOX-cPEG flake-treated cells was determined after 24 h incubation.

Live/dead assay and cell cycle analysis. PC3, DU145 and LNCaP cells (1×10^5 cells per well) were seeded in 12-well plates and incubated for 48 h. The treatment was performed with nGO@cPEG and nGO@DOX-cPEG flakes including free DOX, with or without NIR irradiation, for an additional 24 h. The cells were stained with acridine orange and propidium iodide in PBS at final concentrations of 6.7 and 750 μM, respectively, and photographed using a fluorescence microscope (Eclipse Ti, Nikon Instruments Inc., Melville, NY, USA). A cell cycle analysis of untreated and treated cells (nGO@cPEG and nGO@DOX-cPEG flakes including free DOX, with or without NIR irradiation) was performed using the Cell Clock Assay kit (Biocolor Ltd., County Antrim, UK), which can be used for live-cell detection and analysis of the four major phases (G1, S, G2 and M) of the mammalian cell cycle during *in vitro* culture. Live cancer cells in 12-well plates were treated with redox dye (cell-clock dye reagent) for 1 h at 37 °C and images were taken using a DMIL LED microscope (Leica Microsystems Ltd.). The cell cycle images were used for qualitative evaluation of the apoptosis in cells treated with free DOX and other formulations.

Western blot analysis. PC3, DU145 and LNCaP cells were separately seeded in six-well plates and incubated for 48 h. The cells were treated with nGO@DOX-cPEG flakes, with or without NIR irradiation, and incubated for 24 h. The cells were collected, lysed, treated with proteinase inhibitors and incubated for 40 min on ice. The mixture was centrifuged at 13 000 r.p.m. for 20 min at 4 °C, the supernatant was collected and the protein concentration was quantified using a bovine serum albumin protein assay kit (Thermo Scientific). The protein separation was performed on a 10% bis–Tris polyacrylamide gel (at 210 mA for 120 min) and then transferred to a polyvinylfluoride membrane. After blocking with a 5% nonfat milk powder suspension in Tris-buffered saline and Tween, the membranes were incubated overnight with bax, bcl2, p53, p21 and cleaved-caspase 3 (c-caspase 3) antibodies (Santa Cruz Biotechnology, Inc., Dallas, TX, USA). The samples were incubated with the secondary antibodies for 1 h and photographed using enhanced chemiluminescence.

Biodistribution measurement and in vivo photothermal imaging. The biodistribution of cyanin 5.5 (Cy5.5, fluorescent probe) upon intravenous admisitration (i.v.) of nGO@Cy5.5-cPEG flakes in PC3 tumor-bearing mice was analyzed to track the distribution of flakes within the body. Free Cy5.5 was used as a control. The distributions of free Cy5.5 and nGO@Cy5.5-cPEG were measured at 0, 4, 8 and 24 h following i.v. using the *in vivo* imaging apparatus (FOBI, NeoScience Co., Ltd, Seoul, Korea). Mice were killed after 24 h, and the tumor tissues and organs (heart, lung, liver, spleen and kidney) of each mouse were analyzed to determine the accumulation of Cy5.5 from free Cy5.5 and nGO@Cy5.5-cPEG treatments. *In vivo* photothermal imaging upon i.v. of nGO@DOX-cPEG flakes was performed with digital thermal camera photographs (Therm-App TH, Israel). Briefly, mice were treated (that is, i.v.) with saline or the nGO@DOX-cPEG dispersion, and the tumors were irradiated with an 808 nm NIR laser (2.0 W cm^{-2}) for up to 5 min after 24 h on i.v. Digital imaging was performed to determine the photothermal effects.

In vivo antitumor effect. The *in vivo* antitumor effects of nGO@DOX-cPEG flakes were evaluated in PC3 tumor-bearing Balb/c nude mice. The tumor xenograft model was developed by subcutaneous injection of 2×10^7 PC3 cells into the right flanks of the mice thighs. The tumors were allowed to grow, and the experiments were started once the tumor volumes reached ~ 100 mm^3. The mice were divided into one control and three experimental groups (group 1: control; group 2: DOX-treated; group 3: nGO@DOX-cPEG-treated; group 4: nGO@DOX-cPEG+NIR-treated). Each group comprised eight mice, and the DOX injection was 1 mg kg^{-1} to each mouse. The control group was treated with saline. The treatments were performed via tail vein injection three times (every 3 days). The length and width of the tumors in each group were measured using a Vernier caliper, and the volume was calculated using the formula Volume $= \frac{(\text{length}\times\text{width}^2)}{2}$. Changes in body weights were analyzed for the assessment of toxicities following treatment. The mice were killed using a CO_2 inhalation method and the tumors were surgically collected, fixed in formalin and processed for immunohistochemical assays. All the animal care and experimental protocols were performed in accordance with the guidelines of the Institutional Animal Ethical Committee, Yeungnam University, Republic of Korea.

Histopathological characterization. The xenografted PC3 tumors were serially sectioned (3–4 μm), stained with hematoxylin and eosin and examined for histopathological analysis using optical microscopy (Nikon Corporation, Tokyo, Japan). The tumor cell volumes and intact tumor cell-occupied regions (%mm^{-2} of tumor mass) were calculated using a computer-based automated image analyzer (*i*Solution FL version 9.1, IMT *i*-solution, Inc., Cicero, NY).

Immunohistochemistry. The changes in tumor expression levels of caspase-3, poly(-ADP-ribose) polymerase (PARP), CD31 and Ki-67 were analyzed using antibodies with avidin–biotin peroxidase complex and peroxidase substrate kit (Vector Laboratories, Burlingame, CA, USA). Briefly, endogenous peroxidase activity and nonspecific binding of immunoglobulin were blocked by incubating sections in methanol and 0.3% H_2O_2 for 30 min and incubation in a normal horse serum blocking solution for 1 h in a humidified chamber after heat-induced (95–100 °C) epitope retrieval in 10 mM citrate buffer (pH 6.0). Primary antisera were treated overnight at 4 °C and incubated with biotinylated universal secondary antibody and avidin–biotin peroxidase complex reagents for 1 h at room temperature. All sections were rinsed with 0.01 M PBS solution (three times) between each step. Samples were regarded as testing positive for apoptosis if they were covered by 20% or more of each marker of apoptosis (caspase-3 and PARP). The area occupied by caspase-3 and PARP-positive cells located in a tumor mass was measured using an automated image analyzer (% mm^{-2} of tumor mass).

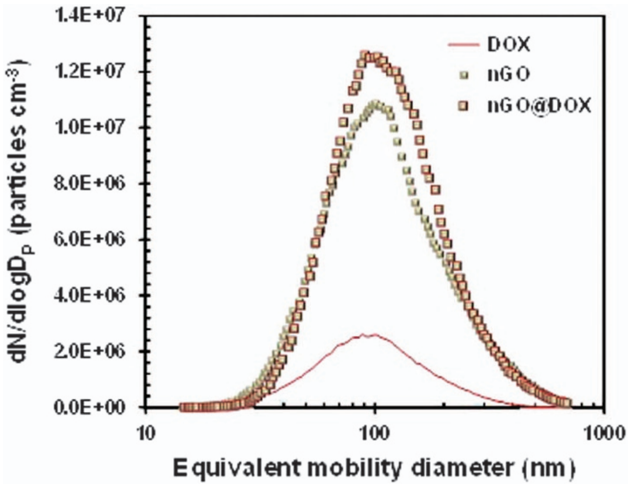

Figure 2 Particle size distributions of nanodimensional graphene oxide (nGO)-incorporated doxorubicin (DOX) (nGO@DOX) flakes including individual nGO flakes and DOX particles.

Statistical analysis. The results are expressed as the mean ± s.d. Student's *t*-test (for pairs of groups) and one-way analysis of variance (for multiple groups) were used to determine the level of statistical significance between the groups, and $P<0.05$ was considered statistically significant.

RESULTS AND DISCUSSION

A scanning mobility particle sizer (3936, TSI, Shoreview, MN, USA) was used to measure the size distribution of nGO@DOX flakes in the gas phase, including individual nGO flakes and DOX particles (Figure 2). The measurements for the nGO@DOX flakes were 113.3 nm (geometric mean diameter), 1.72 (geometric s.d.) and 7.4×10^6 cm^{-3} (total number concentration; Supplementary Table S1). The geometric mean diameter, geometric s.d. and total concentration of the nGO flakes were 108.5 nm, 1.81 and 6.6×10^6 cm^{-3}, respectively, and 94.0 nm, 1.79, and 1.5×10^6 cm^{-3}, respectively, for the DOX particles. The nGO@DOX flakes were larger than individual nGO flakes because of the deposition of DOX components on nGO surfaces during solvent extraction from the hybrid droplets (Figure 1). The significant changes in mechanical properties, such as pressure, velocity and density, were caused by the hybrid droplets that passed through the atomizer orifice, which may redistribute the DOX particles on nGO surfaces and result in no significant size increases of nGO flakes after DOX incorporation. There were no newly formed peaks (that is, multimodal size distribution). The distribution followed that of individual nGO rather than DOX, which indicated that the concentration of nGO flakes was sufficient to support self-assembly of all the DOX particles.

Physicochemical characterizations of the nGO@DOX flakes were performed, as shown in Supplementary Figure S2. Digital images of the nGO, DOX and nGO@DOX dispersions suggested feasibility in single-pass loading of DOX on nGO flakes through visual inspection (red color of DOX in Supplementary Figure S2A). UV–Vis spectroscopy was applied to confirm DOX loading on the nGO flakes (Supplementary Figure S2B). A strong absorption peak at 232 nm and shoulder peak at 302 nm for nGO corresponded to π–π^* transitions and n–π^* transitions of the C = C and C = O groups, respectively, and these peaks verified the gas-phase synthesis of nGO.[27] DOX possesses a characteristic $\lambda_{\max}$ at 480 nm.[28] This peak was also observed in the nGO@DOX dispersion, thereby supporting that DOX incorporation with nGO flakes did not change the optical properties of the nGO (no significant peak changes at 232 and 302 nm). Fourier transform infrared measurements were performed, as presented in Supplementary Figure S2C. The nGO flakes presented characteristic peaks at 1400, 1735, 1160 and 3400 cm^{-1} for C–O bending, C = O stretching in carboxyl groups, C–O stretching vibration in hydroxyl groups and O–H stretching, respectively.[29] The characteristic DOX peaks appeared from 800 to 1900 cm^{-1}, representing the anthracene nucleus and molecular bone vibration of DOX at 1795 cm^{-1}, accompanied with –NH and –OH stretching vibrations at 2915 and 3325 cm^{-1}, respectively.[30,31] These characteristic nGO and DOX peaks were evident in the nGO@DOX flakes, suggesting their quantitative incorporation during self-assembly. The EE and LC of DOX on nGO flakes were determined using high-performance liquid chromatography (Supplementary Figure S2D). High EE (~90%) and LC (~70%) of DOX were observed, and these values were attributed to a strong π–π interaction between the nGO surfaces and DOX molecules caused by a large surface area (Supplementary Figure S3) for the loading.[32] Textural property measurements revealed that the adsorbed nitrogen volume of nGO was significantly larger than that of commercial lateral microdimensional GO (2.2 ± 0.72 μm lateral dimension; inset of Supplementary Figure S3). The specific surface

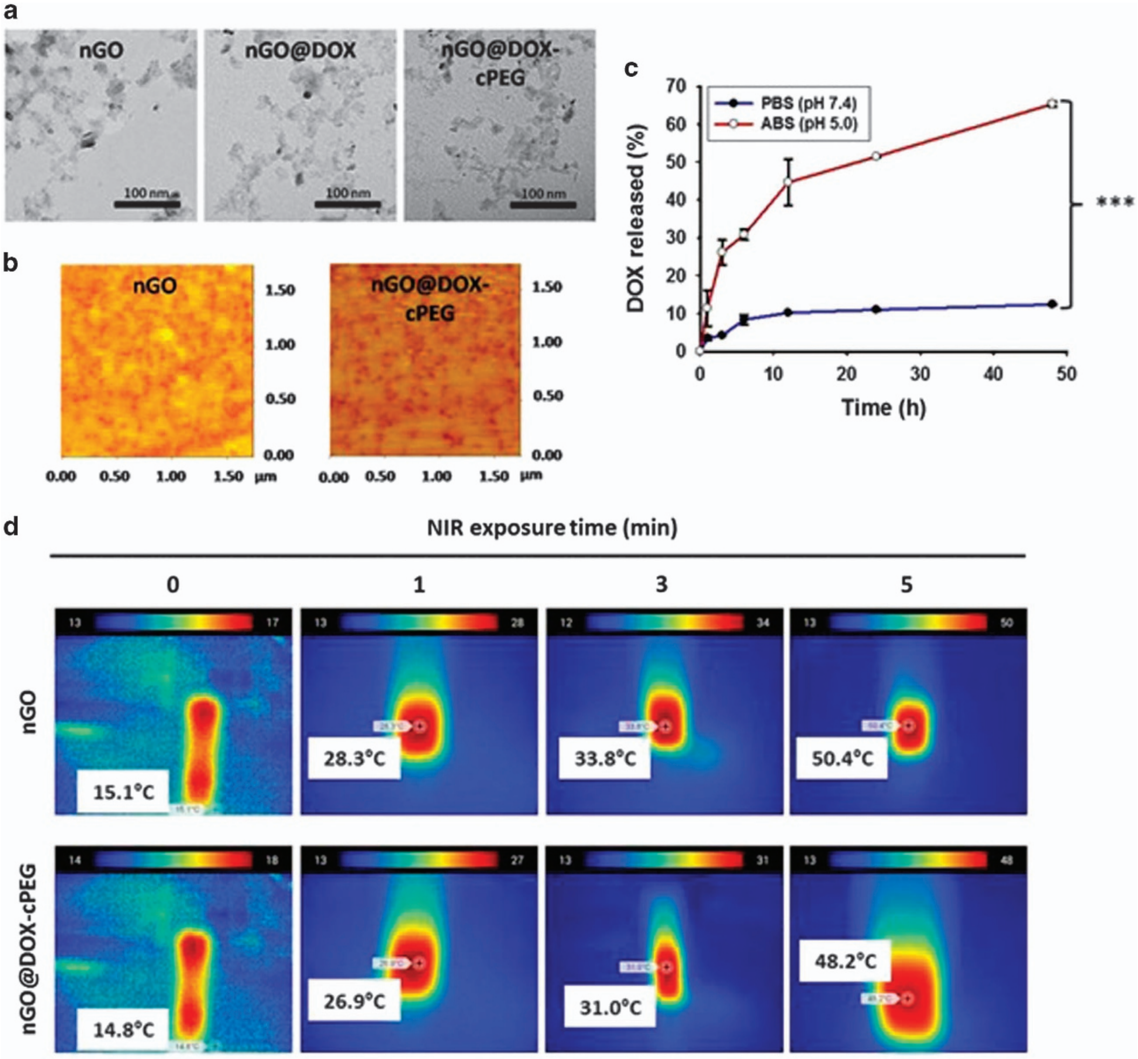

Figure 3 (**a**) Transmission electron microscopy and (**b**) atomic force microscopy images of nGO and nGO@DOX-cPEG flakes. (**c**) *In vitro* release profiles of DOX at different pH conditions ($P<0.01$). (**d**) Effect of NIR on temperature elevations for the nGO and nGO@DOX-cPEG dispersions at different irradiation times. cPEG, chitosan-polyethylene glycol; DOX, doxorubicin; nGO, nanodimensional graphene oxide.

area (581.3 $m^2 g^{-1}$) and pore volume (2.43 $cm^3 g^{-1}$) of our nGO were larger than those of microdimensional GO flakes (43.3 $m^2 g^{-1}$ and 0.16 $cm^3 g^{-1}$), which were examined using a porosimeter (ASAP 2010, Micromeritics Inc.; Supplementary Information). This implied that nGO may be more suitable for high drug loading in GO-based drug delivery applications. To enhance the dispersion stability, cPEG was incorporated[25] with nGO@DOX flakes to prepare the nGO@DOX-cPEG flakes for appropriate chemothermal anticancer assessments; DOX covered the oxygen-containing functional groups (OH, COOH and C=O) on nGO surfaces that are responsible for maintaining aqueous dispersibility.[33] Importantly, this incorporation can minimize macrophage opsonization and increase the blood circulation time for efficient delivery to the tumor area.[25] On the basis of the zeta potential measurements, 20 w/w% was chosen for effective capping of the nGO@DOX flakes because the charge reversal was maximized at this condition. No significant increases in positive potential were noted above this level (Supplementary Figure S4A). The negative potentials of nGO flakes decreased upon DOX incorporation because DOX passivates the oxygen-containing functional groups on the nGO flakes; furthermore, the amine groups in DOX may neutralize the negative charges on nGO surfaces (Supplementary Figure S4B).[34] cPEG incorporation further changed the zeta potential of nGO@DOX flakes to positive polarity, which may be due to the additional incorporation of amine groups from the chitosan matrix.[35] The effects of cPEG incorporation on the EE and LC of DOX were also evaluated (Supplementary Figure S4C). A slight decrease in the EE and LC was observed, which possibly resulted from the sonication used for cPEG incorporation, which caused partial detachment of DOX from the nGO surfaces. Most of the DOX remained on the nGO surfaces even after sonication because of electrostatic attraction and capillary forces between nGO and DOX. Increasing the surface area by decreasing the lateral dimension of the GO flakes may increase the forces that maintain the high EE and LC of DOX on GO flakes. The dispersibility of nGO@DOX and nGO@DOX-cPEG flakes was observed using digital imagery, as presented in Supplementary Figure S4D. Fourier transform infrared analyses presented the appearance of the characteristic cPEG peaks in nGO@DOX-cPEG flakes, suggesting incorporation of the nGO@DOX flakes and cPEG components (Supplementary Figure S4E). The nGO@DOX flakes showed agglomeration and caused instability that was moderated via

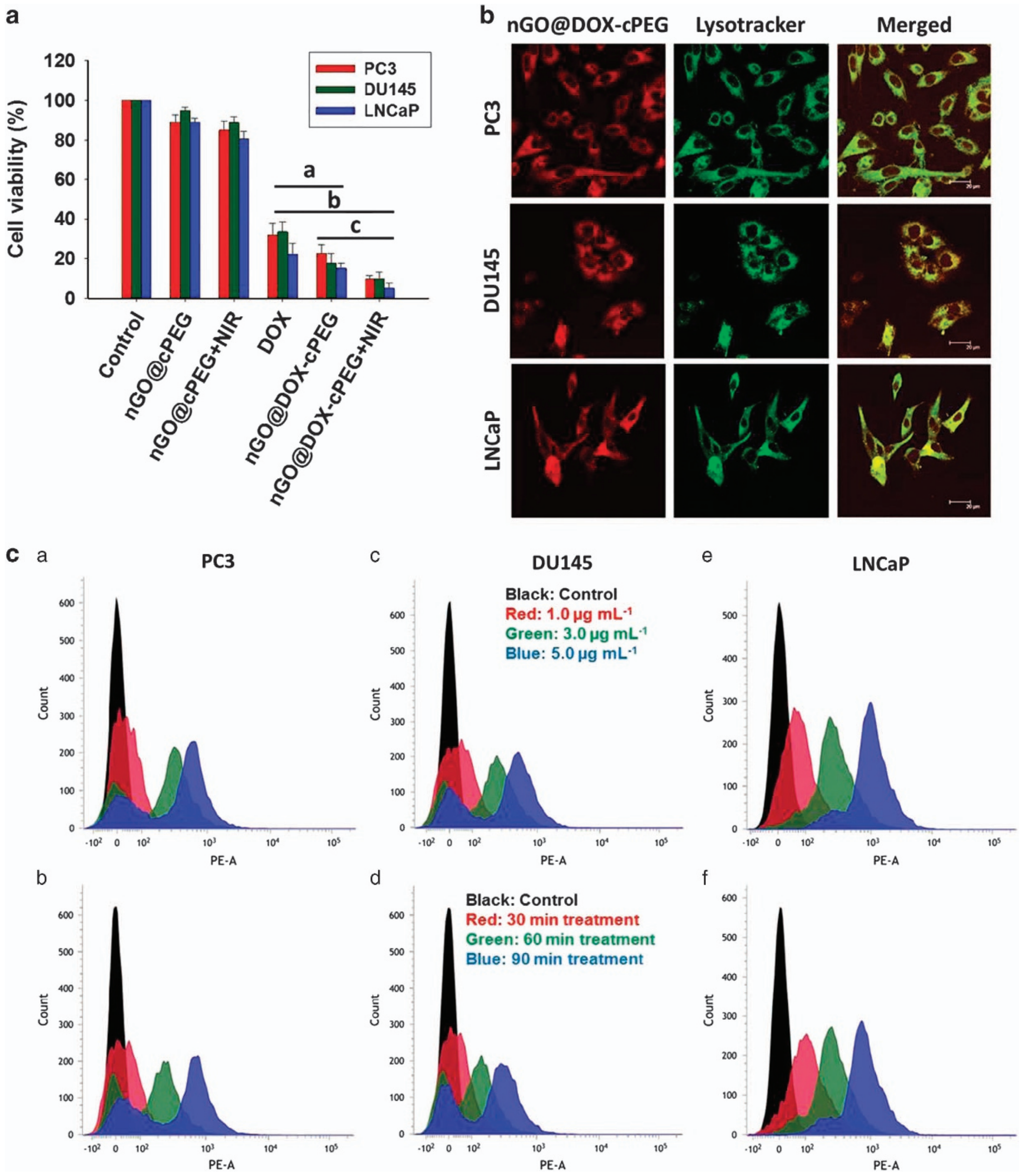

Figure 4 (**a**) Viabilities of PC3, DU145 and LNCaP cells from treatments with nGO@cPEG and nGO@DOX-cPEG flakes including free DOX and with or without NIR exposure (a: $P<0.05$; b: $P<0.01$; c: $P<0.05$). (**b**) Confocal images of PC3, DU145 and LNCaP cells following treatment with nGO@DOX-cPEG flakes. Lysotracker green was used for tracking lysosomes. Scale bar, 30 µm. (**c**) Fluorescence-activated cell sorting measurements for quantitative cellular uptake analyses of nGO@DOX-cPEG flakes using PC3, DU145 and LNCaP cells in a concentration- (a, c, e) and time-dependent manner (b, d, f). cPEG, chitosan-polyethylene glycol; DOX, doxorubicin; nGO, nanodimensional graphene oxide; NIR, near-infrared.

cPEG incorporation, which passivated the surfaces of the nGO@DOX flakes to introduce electrostatic repulsive forces between the same polarity surfaces, maintaining the stability for long-term storage (Supplementary Figure S5). This phenomenon may offer a useful protocol for using gas-phase-assembled drug-loaded nanoplatforms for practical delivery applications.

To clarify the fully nanodimensional characteristic, morphological analyses of the nGO and nGO@DOX-cPEG flakes were performed using transmission electron microscopy (Figure 3a) and atomic force microscopy (Figure 3b). The analyses showed that the lateral dimension of single nGO and nGO@DOX-PEG flakes ranged from 30 to 40 nm (<3.0 nm in thickness; Supplementary Figure S6), which was consistent with the sizes determined through dynamic light scattering (~30 nm). However, these sizes were smaller than those from scanning mobility particle sizer measurements (Figure 2) because the particle diffusion coefficients in the gas phase were three orders of magnitude larger than those encountered in the liquid phase, thereby leading to agglomeration (that is, making some connections between single flakes; Figure 3a and b) between flakes in the gas phase. The drug release profiles (Figure 3c) of DOX from nGO@DOX-cPEG flakes under different pH conditions were evaluated using dialysis. Drug release was significantly higher under acidic conditions than under normal physiological pH, which favored tumor-targeted DOX release. Protonation of DOX under acidic conditions, resulting in a more hydrophilic form, might have led to this result.[36] Effects of NIR irradiation on temperature changes in nGO and nGO@DOX-cPEG

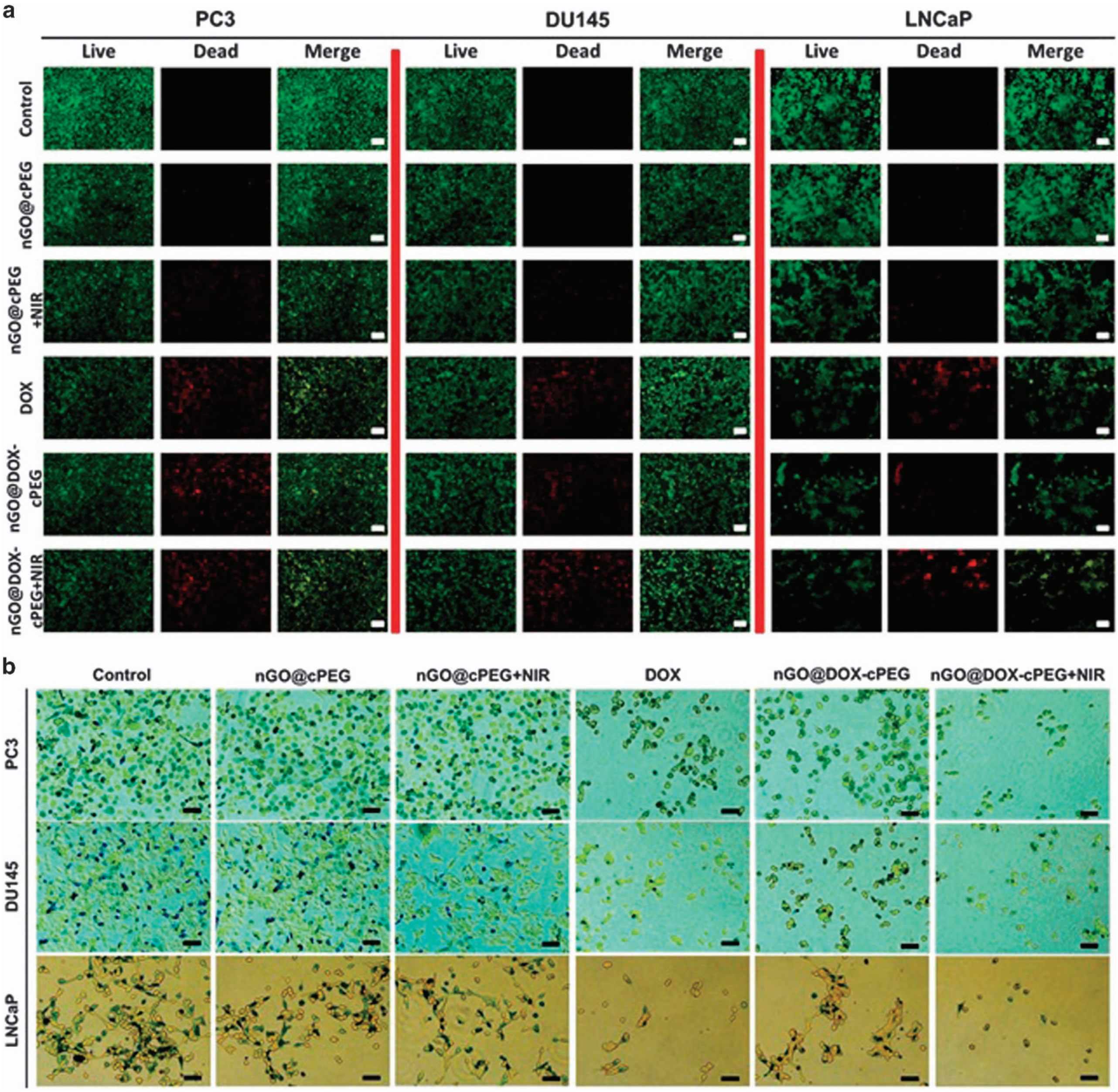

Figure 5 (**a**) Live/dead assay, and (**b**) cycle analysis of PC3, DU145 and LNCaP cells from treatments with nGO@cPEG and nGO@DOX-cPEG flakes including free DOX, with or without NIR irradiation (scale bar: 100 μm). cPEG, chitosan-polyethylene glycol; DOX, doxorubicin; nGO, nanodimensional graphene oxide; NIR, near-infrared.

dispersions were evaluated, as presented in Figure 3d; GO can increase temperature by energy transfer through π-network restoration-mediated light absorption to heat.[37] The temperature increase patterns of the two dispersions were similar during NIR irradiation (0–5 min) and the local temperature reached ~50 °C for nGO@DOX-cPEG flakes. This temperature increase may lead to combined anticancer activity with DOX.

We investigated the chemothermal effects of GO@DOX-cPEG flakes on prostate cancer cells (PC3, DU145 and LNCaP cells), as presented in Figure 4a. Even though the GO@cPEG flakes did not show significant effects in killing the cancer cells, NIR irradiation on the flakes resulted in an increase in the number of dead cells. With DOX treatment, ~60% of cells were damaged and recorded as dead and these cells were increased by ~80% when treated with GO@DOX-cPEG flakes. This scenario may be due to a roll-up effect of nGO flakes (the reduction in total free energy due to π–π interaction existing in the overlap region of the nGO flakes in the present case;[38] Figure 3a and b; the lateral dimension of single nGO flakes decreased upon incorporation of DOX-cPEG) through interaction between nGO and DOX-cPEG. This interaction may enhance the flakes that enter cells for targeted DOX release. The cellular uptake of nGO@DOX-cPEG flakes in prostate cancer cells is presented in Figure 4b. The nGO@DOX-cPEG flakes were efficiently uptaken in the lysosomes of all the prostate cancer cells. Lysosomes, which exist at pH 4.5–5.0, could assist in DOX release inside the cells for targeted therapy.[39] Quantitative cellular uptake of nGO@DOX-cPEG flakes was performed using fluorescence-activated cell sorting (Figure 4c). In all three cell lines, nGO@DOX-cPEG flakes were uptaken in a

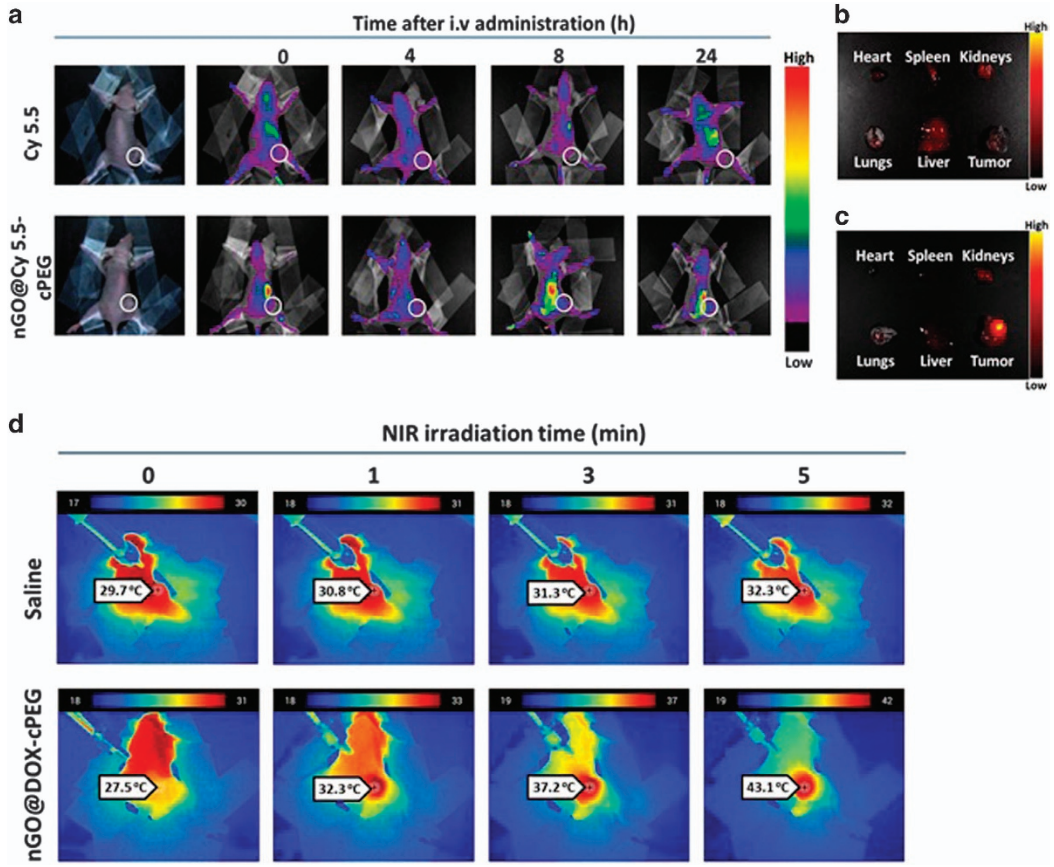

Figure 6 (**a**) *In vivo* biodistribution of nGO@DOX-cPEG in PC3 tumor xenograft mice (circle represents tumor area). Contours (concentration distribution) extracted from individual organs with (**b**) free Cy5.5 and (**c**) nGO@Cy5.5-cPEG are shown. (**d**) *In vivo* photothermal imaging upon NIR laser irradiation on tumors of mice pretreated with saline or nGO@DOX-cPEG. cPEG, chitosan-polyethylene glycol; Cy5.5, cyanin 5.5; DOX, doxorubicin; nGO, nanodimensional graphene oxide; NIR, near-infrared.

concentration- and time-dependent manner. These results support further investigation of the flakes for *in vivo* study.

The apoptotic effects of nGO@DOX-cPEG flakes as a result of chemothermal effects in prostate cancer cells are presented in Supplementary Figure S7A. Consistent with the MTS assay results, analysis of apoptosis revealed better effects of nGO@PEG flakes upon NIR irradiation. DOX treatment has more apoptotic cells because of its known anticancer effects. This effect was further improved in the case of DOX incorporation with nGO flakes, as evidenced by the increase in the number of cells in the late apoptotic region. This result was further improved by a hyperthermia effect of nGO flakes caused by prolonged NIR irradiation for 5 min. These results were confirmed by western blot analyses (Supplementary Figure S7B). Compared with free DOX, enhanced expression of different pro-apoptotic proteins such as bax, p53, p21 and c-caspase 3[25] proved the effectiveness of nGO@DOX-cPEG flakes for tumor-specific delivery mediated by lysosomes. NIR irradiation maximized their expression levels and supported the combined hyperthermia effect of nGO flakes for antitumor therapy.

The cytotoxicities of free DOX, nGO@cPEG and nGO@DOX-cPEG with or without NIR irradiation were evaluated via live/dead assay with PC3, DU145 and LNCaP cell lines (Figure 5a). As expected, the free DOX treatment introduced a significant cell death, as indicated by red dots. The nGO@cPEG flakes exhibited only a small number of dead cells from the treatment, and NIR irradiation introduced slight increases in cell death for all the cell lines. Because of the added DOX, nGO@DOX-cPEG flakes showed a significantly larger number of dead cells than the nGO@cPEG flakes. NIR irradiation introduced further increases in cell death, implying that the photoinduced temperature increase of nGO flakes can effectively accelerate the induction of cellular apoptosis. This may be due to a synergistic effect of photothermal cell killing and DOX release acceleration, suggesting that DOX-cPEG incorporation with nGO flakes would be a suitable formulation for chemothermal cancer therapy. Cell cycle analyses were used to validate the synergistic effect of nGO@DOX-cPEG flakes with or without NIR irradiation on the cell lines (Figure 5b). The untreated groups presented cells in different phases (G1, S, G2 and M) of the cell cycle. Treatment with nGO@cPEG flakes did not significantly alter the cell cycle, and NIR irradiation led to a slight decrease in the number of cells due to photothermal cell death, which is analogous to the live/dead cell assay. Treatments with free DOX and nGO@DOX-cPEG induced G2/M cell cycle arrest in the cell lines with significant decreases in the number of live cells. NIR irradiation introduced further decreases in the number of live cells, and this cycle pattern is consistent with the results presented in Figures 4a and 5a, showing reproducibility of the anticancer effects.

The *in vivo* biodistribution of free Cy5.5 (fluorescent probe) and nGO@Cy5.5-cPEG is presented in Figure 6a. The contours of Cy5.5 concentration as a function of elapsed time after an i.v. showed a tumor accumulation of nGO@Cy5.5-cPEG, but this trend was not observed for the free Cy5.5. However, there was a re-increase in dye concentration from 4 to 8 h, which might be due to fluorescence

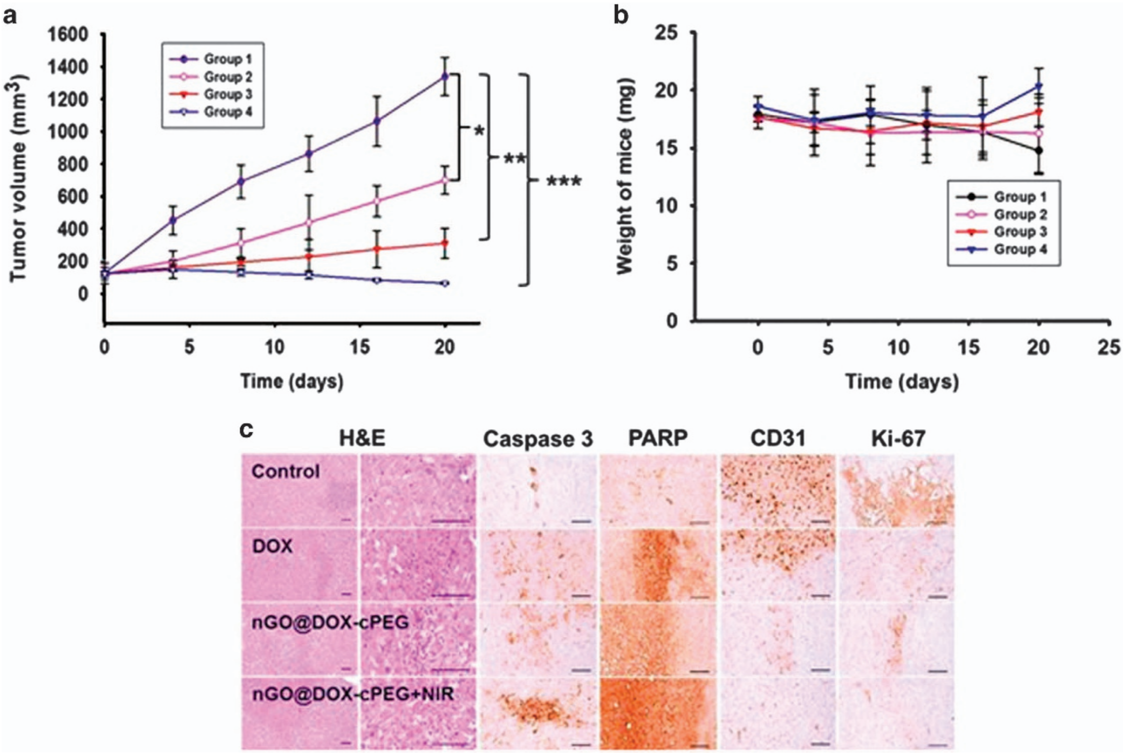

Figure 7 (**a**) Tumor volume and (**b**) body weight comparisons of mice following intravenous administration of different samples (that is, control, DOX, nGO@DOX-cPEG and nGO@DOX-cPEG+NIR) in PC3 tumor-bearing BALB/c nude mice. Each sample was administered three times at 3-day intervals ($^*P<0.05$, $^{**}P<0.01$, $^{***}P<0.001$). (**c**) Immunohistopathological and immunohistochemical analyses. Representative changes in tumor histopathology and immunoreactivity to caspase-3, PARP, CD31 and Ki-67 in tumor masses of nude mice from treatments are shown. Caspase-3 and PARP are markers for apoptosis and CD31 and Ki-67 are markers for angiogenesis. Scale bar, 120 μm. cPEG, chitosan-polyethylene glycol; Cy5.5, cyanin 5.5; DOX, doxorubicin; nGO, nanodimensional graphene oxide; NIR, near-infrared; PARP, poly(-ADP-ribose) polymerase.

quenching when the dye is distributed deeper in the body under physiological conditions.[40] During 4 h following i.v., free Cy5.5 and nGO@Cy5.5-cPEG might have been distributed into deeper tissues; a longer circulation (>4 h) then led to the surface appearance of dye, which might cause the unusual increase pattern. Figure 6a also shows a longer circulation of Cy5.5 for the nGO@Cy5.5-cPEG than that of the free Cy5.5, which may be due to the PEGylated surface of the flakes that could be helpful to extend the delivery and accumulation of the flakes into targeted tumor tissues. The PEGylated surface prevents opsonization;[25] thus, it prolongs the blood circulation time to maintain enhanced fluorescence by nGO@Cy5.5-cPEG. Free Cy5.5 is known to be easily degraded and cleared from the body,[41] resulting in lower fluorescence. The duration for biodistribution analysis was 24 h, and the circulation of flakes could reach a higher extent in tumors at an extended time course (that is, >24 h). However, the instability of Cy5.5 limited the evaluation period to 24 h. The *ex vivo* fluorescence of tumors and organs (liver, lung, spleen, heart and kidney) was subsequently analyzed. The free Cy5.5 case did not exhibit a significant accumulation in the tumor tissues in comparison with other organs (Figure 6b). A site-selective accumulation of Cy5.5 was clearly observed for the flakes in tumor tissues 24 h after i.v., which could be an enhanced permeation and retention effect from the PEGylation of nGO@DOX (that is, cPEG incorporation; Figure 6c). Furthermore, some fluorescence was observed even in mouse skin, which is consistent with a previous report.[42] The fluorescence observed on the organs and tumor was a relative expression that compares fluorescence among the tested organs and tumor only; it was not the fluorescence in the circulation or in the skin. The easy degradation and clearance of free Cy5.5 from the body could be proven from the clear accumulation of free Cy5.5 in the liver and kidneys. A nominal accumulation of free Cy5.5 was also observed in tumors, implying that more accumulation of nGO@Cy5.5-cPEG occurred in tumors with a relatively lower accumulation in the liver and kidney from the longer blood circulation and suppressed opsonization, resulting in a higher chance of reaching the tumor site. *In vivo* imaging upon i.v. of nGO@DOX-cPEG flakes to validate a more realistic photothermal effect was performed in a PC3 xenograft mouse model. At 24 h after i.v. via the tail vein, the tumors were irradiated with an 808 nm NIR laser ($2.0\ \mathrm{W\,cm^{-2}}$) for up to 5 min (Figure 6d). There was no significant thermal elevation for mice treated with saline only. In the case of nGO@DOX-cPEG flakes, the treated mice presented a significant thermal elevation from 27.5 to 43.1 °C in the focal region. No obvious temperature changes were observed for the non-irradiated body parts during the test. Even though NIR light can only penetrate a few millimeters into biological systems,[43] the results showed pronounced anticancer effects under NIR irradiation that are likely due to the high targeting efficiency of nGO@DOX-cPEG. However, in an actual clinical situation, it would be challenging to apply enough NIR energy to tumor sites located deep inside the body. A potential suitable approach for such conditions is the use of minimally invasive surgical tools.[41] A combination of advanced electronics and fluorescence-labeled nanosystems can enable fluorescence-based mapping, pH sensing and localized photo/chemotherapy for efficient cancer treatments.[44]

On the basis of the *in vitro* assessments, we attempted to verify the anticancer activity of the assembled nGO@DOX-cPEG flakes using an *in vivo* mouse xenograft model. Following subcutaneous tumor injection (PC3 cells) and growth up to 100 mm^3, treatment with free DOX and the flakes was performed via tail vein injections. NIR irradiation at the tumor site was used to determine the chemothermal effects on tumor inhibition. Compared with the control and free DOX groups, the nGO@DOX-cPEG flakes remarkably facilitated the inhibition of tumor growth, which was further suppressed by NIR irradiation at the tumor site. After a 20-day treatment, the antitumor activity was in the order of nGO@DOX-cPEG+NIR > nGO@DOX-cPEG > DOX when they were compared with the untreated control (Figure 7a). The safety profiles of the free DOX and flakes were analyzed by measuring body weights (Figure 7b). Mice treated with the control and free DOX groups showed body weight losses of ~18 and 12%, respectively, whereas no clear correlations were found between the number of treatment days and weight loss for the nGO@DOX-cPEG and nGO@DOX-cPEG+NIR groups. In the control group, the results might be attributed to metastases of the tumor cells that possibly affected multiple organs in mice, thereby inducing clear weight losses. The results for the free DOX group could be related to the previously reported toxicities that cause weight loss in mice, such as cardiotoxicity, neurotoxicity and nephrotoxicity.[45–47] Unlike the control and free DOX groups, the enhanced anticancer effects and reduced toxicities from application of the nGO@DOX-cPEG flakes (Supplementary Figure S8) led to accumulation and efficient delivery of DOX to tumor sites, which may be due to the sustained release and prolonged circulation in the bloodstream and the enhanced permeation and retention effect.[47,48] In addition, histopathological and immunohistochemical analyses were performed on the tumor masses to determine the expression levels of caspase-3, PARP, CD31 and Ki-67 (Figure 7c; Supplementary Table S2). The tumor cell volumes after nGO@DOX-cPEG treatment were significantly smaller than those of free DOX, and the volumes were further reduced by NIR irradiation. The expression of apoptotic markers caspase-3 and PARP was more clearly illustrated for nGO@DOX-cPEG- and nGO@DOX-cPEG+NIR-treated tumors than those for the control and free DOX-treated groups, whereas a reverse tendency was found for CD31 (an angiogenesis marker) and Ki-67 (a tumor proliferation marker) because of the enhanced accumulation of the fully nano-dimensional flakes followed by DOX release at the tumor sites. These results indicated that the anticancer effects of the flakes were better than those of free DOX and that NIR irradiation further enhanced prostate cancer treatment due to chemothermal activity.

As a core portion of desired nanoplatforms, nGO@DOX flakes were conveniently assembled in a single-pass gas-phase condition. They were incorporated with cPEG to form nGO@DOX-cPEG flakes in an on-demand configuration for NIR-induced anticancer therapy. The nGO flakes exhibited high and stable DOX-loading capacity and pH-dependent drug release profiles for cancer treatment. Measurements of the *in vitro* cellular uptake and apoptosis in prostate cancer cells demonstrated the effectiveness of nGO@DOX-cPEG flakes, which introduced the combined effects of DOX release and hyperthermia under NIR irradiation. *In vivo* study revealed that the fully lateral nanodimensional systems could enhance accumulation at the tumor sites to activate sustained release and prolonged circulation with enhanced permeation and retention for improved antitumor effects and safety. Thus, the proposed approach may enable the on-demand continuous assembly and modification of fresh multi-modal nanoplatforms for use in various drug delivery systems, including theranostic applications.

CONFLICT OF INTEREST

The authors declare no conflict of interest.

ACKNOWLEDGEMENTS

This research was supported by a National Research Foundation of Korea (NRF) grant funded by the Korean government (MSIP; No 2015R1A2A2A04005809, 2015R1A2A2A01004118 and 2015R1A2A2A04004806). This work was also supported by the Medical Research Center Program (No 2015R1A5A2009124) through the NRF funded by MSIP.

Author contributions: RKT performed the experiments and wrote the manuscript. SKK supported the *in vivo* experiments and the manuscript preparation. JHB, CSY and JOK conceived of the project, designed and performed the experiments, and wrote the manuscript.

PUBLISHER'S NOTE

1 Piktel, E., Niemirowicz, K., Wątek, M., Wollny, T., Deptuła, P. & Bucki, R. Recent insights in nanotechnology-based drugs and formulations designed for effective anti-cancer therapy. *J. Nanobiotechnol.* **14**, 39 (2016).

2 Kanamala, M., Wilson, W. R., Yang, M., Palmer, B. D. & Wu, Z. Mechanisms and biomaterials in pH-responsive tumour targeted drug delivery: areview. *Biomaterials* **85**, 152–167 (2016).

3 Lim, E.-K., Kim, T., Paik, S., Haam, S., Huh, Y.-M. & Lee, K. Nanomaterials for theranostics: recent advances and future challenges. *Chem. Rev.* **115**, 327–394 (2015).

4 He, C., Lu, J. & Lin, W. Hybrid nanoparticles for combination therapy of cancer. *J. Control. Release* **219**, 224–236 (2015).

5 Wang, T., Wang, D., Yu, H., Wang, M., Liu, J., Feng, B., Zhou, F., Yin, Q., Zhang, Z., Huang, Y. & Li, Y. Intracellularly acid-switchable multifunctional micelles for combinational photo/chemotherapy of the drug-resistant tumor. *ACS Nano* **10**, 3496–3508 (2016).

6 Wan, H., Zhang, Y., Liu, Z., Xu, G., Huang, G., Ji, Y., Xiong, Z., Zhang, Q., Dong, J., Zhang, W. & Zou, H. Facile fabrication of a near-infrared responsive nanocarrier for spatiotemporally controlled chemo-photothermal synergistic cancer therapy. *Nanoscale* **6**, 8743–8753 (2014).

7 Olejniczak, J., Carling, C.-J. & Almutairi, A. Photocontrolled release using one-photon absorption of visible or NIR light. *J. Control. Release* **219**, 18–30 (2015).

8 Geim, A. K. & Novoselov, K. S. The rise of graphene. *Nat. Mater.* **6**, 183–191 (2007).

9 Novoselov, K. S., Falko, V. I., Colombo, L., Gellert, P. R., Schwab, M. G. & Kim, K. A roadmap for graphene. *Nature* **490**, 192–200 (2012).

10 Yang, X., Zhang, X., Liu, Z., Ma, Y., Huang, Y. & Chen, Y. High-efficiency loading and controlled release of doxorubicin hydrochloride on graphene oxide. *J. Phys. Chem. C* **112**, 17554–17558 (2008).

11 Peng, C., Hu, W., Zhou, Y., Fan, C. & Huang, Q. Intracellular imaging with a graphene-based fluorescent probe. *Small* **6**, 1686–1692 (2010).

12 Yang, K., Feng, L., Shi, X. & Liu, Z. Nano-graphene in biomedicine: theranostic applications. *Chem. Soc. Rev.* **42**, 530–547 (2013).

13 Fu, W. L., Zhen, S. J. & Huang, C. Z. One-pot green synthesis of graphene oxide/gold nanocomposites as SERS substrates for malachite green detection. *Analyst* **138**, 3075–3081 (2013).

14 Liu, J., Cui, L. & Losic, D. Graphene and graphene oxide as new nanocarriers for drug delivery applications. *Acta Biomater.* **9**, 9243–9257 (2013).

15 Yang, K., Zhang, S., Zhang, G., Sun, X., Lee, S.-T. & Liu, Z. Graphene in mice: ultrahigh *in vivo* tumor uptake and efficient photothermal therapy. *Nano Lett.* **10**, 3318–3323 (2010).

16 Yang, K., Wan, J., Zhang, S., Tian, B., Zhang, Y. & Liu, Z. The influence of surface chemistry and size of nanoscale graphene oxide on photothermal therapy of cancer using ultra-low laser power. *Biomaterials* **33**, 2206–2214 (2012).

17 Xu, Z., Wang, S., Li, Y., Wang, M., Shi, P. & Huang, X. Covalent functionalization of graphene oxide with biocompatible poly(ethylene glycol) for delivery of paclitaxel. *ACS Appl. Mater. Interfaces* **6**, 17268–17276 (2014).

18 Li, J., Lyv, Z., Li, Y., Liu, H., Wang, J., Zhan, W., Chen, H., Chen, H. & Li, X. A theranostic prodrug delivery system based on Pt(IV) conjugated nano-graphene oxide with synergistic effect to enhance the therapeutic efficacy of Pt drug. *Biomaterials* **51**, 12–21 (2015).

19 Rauti, R., Lozano, N., León, V., Scaini, D., Musto, M., Rago, I., Ulloa Severino, F. P., Fabbro, A., Casalis, L., Vázquez, E., Kostarelos, K., Prato, M. & Ballerini, L. Graphene oxide nanosheets reshape synaptic function in cultured brain networks. *ACS Nano* **10**, 4459–4471 (2016).

20 McCallion, C., Burthem, J., Rees-Unwin, K., Golovanov, A. & Pluen, A. Graphene in therapeutics delivery: Problems, solutions and future opportunities. *Eur. J. Pharm. Biopharm.* **104**, 235–250 (2016).

21 Conner, S. D. & Schmid, S. L. Regulated portals of entry into the cell. *Nature* **422**, 37–44 (2003).
22 Mu, Q., Su, G., Li, L., Gilbertson, B. O., Yu, L. H., Zhang, Q., Sun, Y.-P. & Yan, B. Size-dependent cell uptake of protein-coated graphene oxide nanosheets. *ACS Appl. Mater. Interfaces* **4**, 2259–2266 (2012).
23 Byeon, J. H., Park, J. H., Yoon, K. Y., Ko, B. J., Ji, J. H. & Hwang, J. Removal of volatile organic compounds by spark generated carbon aerosol particles. *Carbon* **44**, 2106–2108 (2006).
24 Hummers, W. S. & Offeman, R. E. Preparation of graphitic oxide. *J. Am. Chem. Soc.* **80**, 1339–1339 (1958).
25 Thapa, R. K., Youn, Y. S., Jeong, J.-H., Choi, H.-G., Yong, C. S. & Kim, J. O. Graphene oxide-wrapped PEGylated liquid crystalline nanoparticles for effective chemo-photothermal therapy of metastatic prostate cancer cells. *Colloids Surf. B Biointerfaces* **143**, 271–277 (2016).
26 Brunauer, S., Emmett, P. H. & Teller, E. Adsorption of gases in multimolecular layers. *J. Am. Chem. Soc.* **60**, 309–319 (1938).
27 Eda, G. & Chhowalla, M. Chemically derived graphene oxide: towards large-area thin-film electronics and optoelectronics. *Adv. Mater.* **22**, 2392–2415 (2010).
28 Manocha, B. & Margaritis, A. Controlled release of doxorubicin from doxorubicin/gamma-polyglutamic acid ionic complex. *J. Nanomater.* **2010**, 9 (2010).
29 Wang, Y., Liu, K., Luo, Z. & Duan, Y. Preparation and tumor cell model based biobehavioral evaluation of the nanocarrier system using partially reduced graphene oxide functionalized by surfactant. *Int. J. Nanomed.* **10**, 4605–4620 (2015).
30 Madhusudhan, A., Reddy, G., Venkatesham, M., Veerabhadram, G., Kumar, D., Natarajan, S., Yang, M.-Y., Hu, A. & Singh, S. Efficient pH dependent drug delivery to target cancer cells by gold nanoparticles capped with carboxymethyl chitosan. *Int. J. Mol. Sci.* **15**, 8216–8234 (2014).
31 Li, J.-M., Zhang, W., Su, H., Wang, Y.-Y., Tan, C.-P., Ji, L.-N. & Mao, Z.-W. Reversal of multidrug resistance in MCF-7/Adr cells by codelivery of doxorubicin and BCL2 siRNA using a folic acid-conjugated polyethylenimine hydroxypropyl-β-cyclodextrin nanocarrier. *Int. J. Nanomed.* **10**, 3147–3162 (2015).
32 Thapa, R. K., Choi, J. Y., Poudel, B. K., Choi, H. G., Yong, C. S. & Kim, J. O. Receptor-targeted, drug-loaded, functionalized graphene oxides for chemotherapy and photothermal therapy. *Int. J. Nanomed.* **11**, 2799–2813 (2016).
33 Konkena, B. & Vasudevan, S. Understanding aqueous dispersibility of graphene oxide and reduced graphene oxide through pK$_a$measurements. *J. Phys. Chem. Lett.* **3**, 867–872 (2012).
34 Chouhan, R. & Bajpai, A. K. Real time *in vitro* studies of doxorubicin release from PHEMA nanoparticles. *J. Nanobiotechnol.* **7**, 5 (2009).
35 Madrigal-Carballo, S., Rodríguez, G., Sibaja, M., Reed, J. D., Vila, A. O. & Molina, F. Chitosomes loaded with cranberry proanthocyanidins attenuate the bacterial lipopolysaccharide-induced expression of iNOS and COX-2 in raw 264.7 macrophages. *J. Liposome Res.* **19**, 189–196 (2009).
36 Shen, H. J., Shi, H., Ma, K., Xie, M., Tang, L. L., Shen, S., Li, B., Wang, X. S. & Jin, Y. Polyelectrolyte capsules packaging BSA gels for pH-controlled drug loading and release and their antitumor activity. *Acta Biomater.* **9**, 6123–6133 (2013).
37 Sheng, Z., Song, L., Zheng, J., Hu, D., He, M., Zheng, M., Gao, G., Gong, P., Zhang, P., Ma, Y. & Cai, L. Protein-assisted fabrication of nano-reduced graphene oxide for combined *in vivo* photoacoustic imaging and photothermal therapy. *Biomaterials* **34**, 5236–5243 (2013).
38 Wang, X., Yang, D. P., Huang, G., Huang, P., Shen, G., Guo, S., Mei, Y. & Cui, D. Rolling up grapheme oxide sheets into micro/nanoscrolls by nanoparticle aggregation. *J. Mater. Chem.* **22**, 17441–17444 (2012).
39 Thapa, R. K., Choi, J. Y., Poudel, B. K., Hiep, T. T., Pathak, S., Gupta, B., Choi, H.-G., Yong, C. S. & Kim, J. O. Multilayer-coated liquid crystalline nanoparticles for effective sorafenib delivery to hepatocellular carcinoma. *ACS Appl. Mater. Interfaces* **7**, 20360–20368 (2015).
40 Wang, L., Meng, D., Hao, Y., Hu, Y., Niu, M., Zheng, C., Yanyan, Y., Li, D., Zhang, P., Chang, J., Zhang, Z. & Zhang, Y. A gold nanostar based multi-functional tumor-targeting nanoplatform for tumor theranostic applications. *J. Mater. Chem. B* **4**, 5895–5906 (2016).
41 Bouteiller, C., Clavé, G., Bernardin, A., Chipon, B., Massonneau, M., Renard, P. Y. & Romieu, A. Novel water-soluble near-infrared cyanine dyes: synthesis, spectral properties, and use in the preparation of internally quenched fluorescent probes. *Bioconjug. Chem.* **18**, 1303–1317 (2007).
42 Pereira, P., Correia, A. & Gama, F. M. *In vivo* imaging of glycol chitosan-based nanogel biodistribution. *Macromol. Biosci.* **16**, 432–440 (2016).
43 Stolik, S., Delgado, J. A., Pérez, A. & Anasagasti, L. Measurement of the penetration depths of red and near infrared light in human '*ex vivo*' tissues. *J. Photochem. Photobiol. B* **57**, 90–93 (2000).
44 Lee, H., Lee, Y., Song, C., Cho, H. R., Ghaffari, R., Choi, T. K., Kim, K. H., Lee, Y. B., Ling, D., Lee, H., Yu, S. J., Choi, S. H., Hyeon, T. & Kim, D. H. An endoscope with integrated transparent bioelectronics and theranostic nanoparticles for colon cancer treatment. *Nat. Commun.* **6**, 10059 (2015).
45 Joseph, M. M., Aravind, S. R., George, S. K., Pillai, K. R., Mini, S. & Sreelekha, T. T. Galactoxyloglucan-modified nanocarriers of doxorubicin for improved tumor-targeted drug delivery with minimal toxicity. *J. Biomed. Nanotechnol.* **10**, 3253–3268 (2014).
46 Alibolandi, M., Sadeghi, F., Abnous, K., Atyabi, F., Ramezani, M. & Hadizadeh, F. The chemotherapeutic potential of doxorubicin-loaded PEG-b-PLGA nanopolymersomes in mouse breast cancer model. *Eur. J. Pharm. Biopharm.* **94**, 521–531 (2015).
47 Li, X., Yang, X., Lin, Z., Wang, D., Mei, D., He, B., Wang, X., Wang, X., Zhang, Q. & Gao, W. A folate modified pH sensitive targeted polymeric micelle alleviated systemic toxicity of doxorubicin (DOX) in multi-drug resistant tumor bearing mice. *Eur. J. Pharm. Sci.* **76**, 95–101 (2015).
48 Xu, Z., Zhu, S., Wang, M., Li, Y., Shi, P. & Huang, X. Delivery of paclitaxel using PEGylated graphene oxide as a nanocarrier. *ACS Appl. Mater. Interfaces* **7**, 1355–1363 (2015).

Supplementary Information accompanies the paper on the NPG Asia Materials website (http://www.nature.com/am)